Silicon-Reduced Graphene Oxide Self-Standing Composites Suitable as Binder-Free Anodes for Lithium-Ion Batteries

Cristina Botas,[†] Daniel Carriazo,[*,†,‡] Wei Zhang,[†,‡] Teófilo Rojo,[†,§] and Gurpreet Singh[†]

[†]CIC EnergiGUNE, Parque Tecnológico de Álava, Albert Einstein 48, 01510 Miñano, Álava, Spain

[‡]IKERBASQUE, Basque Foundation for Science, 48013 Bilbao, Spain

[§]Departamento de Química Inorgánica, Universidad Del País Vasco UPV/EHU, 48080 Bilbao, Spain

S *Supporting Information*

ABSTRACT: Silicon-reduced graphene oxide (Si-rGO) composites processed as self-standing aerogels (0.2 g cm^{-3}) and films (1.5 g cm^{-3}) have been prepared by the thermal reduction of composites formed between silicon nanoparticles and a suspension of graphene oxide (GO) in ethanol. The characterization of the samples by different techniques (X-ray diffraction, Raman, thermogravimetric analysis, and scanning electron microscopy) show that in both cases the composites are formed by rGO sheets homogeneously decorated with 50 nm silicon nanoparticles with silicon contents of ~40% wt. The performances of these self-standing materials were tested as binder-free anodes in lithium-ion batteries (LIBs) in a half cell configuration under two different galvanostatic charge–discharge cutoff voltages (75 and 50 mV). The results show that the formation of a solid electrolyte interphase (SEI) is favored in composites processed as aerogels due to its large exposed surface, which prevents the activation of silicon when they are cycled within the 2 to 0.075 V voltage windows. It is also found that the composites processed in the form of self-standing films exhibit good stability over the first 100 cycles, high reversible specific capacity per mass of electrode (~750 mAh g^{-1}), areal capacities that reach 0.7 mAh cm^{-2}, and high Coulombic efficiencies (80% for the first charge–discharge cycle and over 99% in the subsequent cycles).

KEYWORDS: *self-assembly, nanoparticles, high density electrodes, energy storage, electrochemistry, nanostructured materials, free-standing electrodes*
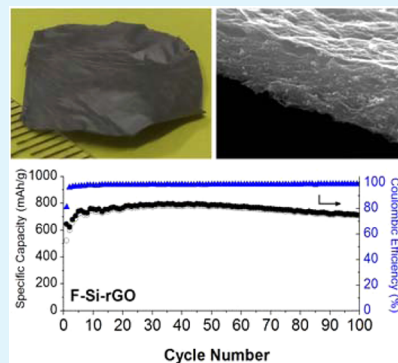
INTRODUCTION

Rechargeable lithium-ion batteries (LIBs) are the dominant electrical energy storage devices in today's portable electronics such as cell phones, laptops or tablets because of their high energy density and low self-discharge rate.[1] However, its prevalent use in large-scale applications such as electric vehicles still requires an improvement in its volumetric energy density, safety, life span, and component's costs. The main strategy to increase the energy density of LIBs is the development of new materials that show improved specific capacities compared with those of materials currently used as electrodes in LIBs.[2,3] Nowadays, commercially available LIBs use carbon in different forms such as graphite or hard carbon as the anode because it is abundant, cheap, has high electronic conductivity (~200 S cm^{-1}), and exhibits a theoretical gravimetric capacity of 372 mA h g^{-1}.[4] Recently, some elements that include silicon, tin, or germanium, have been proposed as potential candidates to replace graphite as high capacity anodes.[5,6]

In fact, silicon is, after oxygen, the most abundant element in earth's crust, is environmentally benign and has a low discharge potential (~0.4 V vs Li/Li$^+$) and a theoretical gravimetric capacity of 3579 mAh g^{-1}. Therefore, it seems to be an excellent candidate to replace graphite as the anode in next generation LIBs.[7−9] However, the extremely high volume expansion (up to a 300%) undergone by silicon particles upon its alloying with lithium and the increasing formation of a solid electrolyte interphase (SEI) can produce capacity fading and electrode disruption, limiting its use as an anode in real devices.[10]

To overcome these issues, different strategies that include the development of advanced binders,[11,12] silicon nanostructuration,[13,14] or its encapsulation in a proper matrix[15−20] have been explored in recent years. Graphene, an allotrope of carbon formed by a two-dimensional (2D) monolayer of carbon atoms arranged in a honeycomb network with outstanding properties such as high electrical conductivity, flexibility and transparency,[21] has been pointed out as an excellent support to disperse or to confine silicon particles.[22,23]

Although the use of graphene as an anode in real energy storage devices could be questioned due to its low density and its high specific surface area, which decreases the volumetric energy density of the whole device[24] and undergoes an enhancement on the SEI formation,[25] graphene sheets would offer silicon a suitable support not only to improve its

electronic conductivity but also to stabilize silicon particles during cycling.[26]

Recently, several works have shown the benefits of using Si-graphene composites as anodes for LIBs.[27−29] Special attention have been received for self-standing silicon-based composites in the form of flexible films or aerogels, which exhibit added value due to their potential application in flexible devices.[30−33]

Different strategies to obtain homogeneous Si-graphene composites, including the use of chemical vapor deposition (CVD) to grow a graphene layers on silicon particles[34] or to deposit nanostructured silicon on the graphene sheets,[35] magnesiumthermic reduction of silica,[36] or chemical routes involving the mixing of both components,[37,38] have been explored. Some of them are complex routes that involve several steps or require high vacuum conditions which are difficult to scale up. Focusing onto the solvent-based routes, previous examples have reported that, to improve the affinity of the Si particles with the aqueous graphene oxide (GO) suspensions, the particles were previously exposed to air, submitted to ultrasonication, or mixed with some additives.[27,39,40] Some of them also included treatment with hydrofluoric acid as an additional step to dissolve a shell of SiO_x (where $x \leq 2$) that was formed during the process.[39,40]

Herein, we present a facile way for the preparation of silicon nanoparticle-reduced graphene oxide (Si-rGO) composites from homemade chemically produced graphene oxide in ethanol and commercial silicon nanoparticles. This very simple approach allowed highly homogeneous Si-GO composites to be obtained while preventing the oxidation of silicon particles. These materials were processed in form of self-standing aerogels and highly dense films ($\sim$1.5 g cm^{-3}), and their performances were evaluated as binder-free anodes for LIBs vs Li in half cell configuration under different cycling conditions.

■ EXPERIMENTAL SECTION

Synthesis of Si-Reduced Graphene Oxide Composites. A GO suspension in ethanol was prepared following a procedure previously described elsewhere[41,42] with some modifications. First, graphite oxide (GrO) was obtained from synthetic graphite provided by IMERYS Graphite & Carbon (TIMREX-SFG75) by a modified Hummers method. This method makes use of the Hummers' reagents with additional amounts of $NaNO_3$ and $KMnO_4$. Briefly, 360 mL of a concentrated H_2SO_4 solution was added into a mixture formed by 7.5 g of synthetic graphite and 7.5 g of $NaNO_3$. The mixture was then cooled using an ice bath. Once the mixture was cooled, 45 g of $KMnO_4$ was slowly added in small doses to keep the reaction temperature below 20 °C. The solution was then heated to 35 °C and stirred for 3 h. After this period, 1.5 L of a H_2O_2 (3% wt) solution was slowly added, giving rise to a pronounced exothermic effect that increased the temperature to 98 °C, and the reaction mixture was further stirred for 1 h. The remaining solid material was washed with different amounts of water and centrifuged again. GO suspension in ethanol of ($\sim$5 mg mL^{-1}) was obtained by washing several times a GrO slurry with dry ethanol, and then the suspension was sonicated for 1 h and centrifuged (3500 rpm, 30 min), after which any remaining solid was discarded. The GO concentration was fixed to $\sim$5 mg mL^{-1} by addition of a certain volume of ethanol.

Silicon-graphene oxide (Si-GO) composites were prepared by mixing 25 mg of silicon nanoparticles (Alfa Aesar) with 20 mL of the GO suspension in ethanol (4.5 mg mL^{-1}) under an argon atmosphere. This suspension was stirred for 2 h. To process the composites as self-standing samples, two different strategies were followed:

For the preparation of the aerogels (A-Si-GO), the alcoholic suspension of GO with Si was evaporated at 30 °C in a rotary evaporator until the volume was reduced to 10% of the initial volume; then, a certain amount of distilled water was added to recover the starting volume, and the mixture was stirred for 1 h more. After this time, the suspension was suddenly frozen at −196 °C using liquid nitrogen and then freeze-dried in a Telstar LyoQuest freeze-drier.

Films (F-Si-GO) were obtained by solvent casting a certain amount of a silicon-graphene oxide suspension in ethanol on a silicone rubber mold. A few milliliters of the suspension were drop-casted on silicon rubber and allowed to dry at room temperature under atmospheric pressure.

The thermal reduction of graphene oxide in all samples was accomplished by slow heating in a tubular furnace at 1 °C min^{-1} up to 200 °C to avoid the thermal blasting of GO and then to 1000 °C at 2 °C min^{-1} under a dynamic Ar/H$_2$ (95/5) atmosphere (100 mL °C min^{-1}); finally, they was maintained at this temperature for 1 h. Composite samples obtained after the reduction of graphene oxide composite films and aerogels are hereafter denoted as F-Si-rGO and A-Si-rGO, respectively.

Physicochemical Characterization. X-ray diffraction (XRD) patterns were registered for powdered samples in a Bruker D8 X-ray diffractometer; data were collected at 40 kV and 30 mA using Cu Kα radiation over 2θ within the range from 20 to 70° at steps of 0.02° and residence time of 5 s. Raman spectra were recorded with a Renishaw spectrometer (Nanonics multiview 2000) operating with an excitation wavelength of 532 nm. The spectra were acquired with 10 s of exposition time of the laser beam to the sample. Thermogravimetric curves were obtained by heating the material with a heating rate of 10 °C min^{-1} from 50 to 1000 °C under a dynamic atmosphere of synthetic air in a thermogravimetric balance STA 449 F3 Jupiter model from Netzsch. Scanning electron microscope (SEM) images were acquired in a field emission Quanta 200 FEG microscope from FEI. Fourier transform infrared (FT-IR) spectra of the cycled electrodes were acquired immediately after being disassembled from the coin cells in a VERTEX 70 model from Bruker.

A Tecnai G2 transmission electron microscope (TEM, FEI) was employed for microstructural characterization. The powder samples were ultrasonically dispersed in ethanol for 10 min. Then, several drops of the solution were taken on a holey carbon films supported by Cu for TEM characterization.

Nitrogen adsorption−desorption isotherms were registered in an ASAP2020 instrument from micromeritics. Samples were outgassed at 250 °C during the 3 h prior to the analysis. Specific surface area values were determined using the BET equation within the 0.05−0.2 relative pressure range. The pore size distribution (PSD) was determined by the nonlocal density functional theory (NLDFT) method from the nitrogen adsorption data assuming a slit-shaped pore model.

Electrodes Preparation, Assembly, and Electrochemical Characterization. Electrochemical measurements were carried out in CR2032-type coin cells assembled inside a glovebox under an argon atmosphere. Half cells were fabricated with the Li/separator/samples configuration.

Self-standing discs 11 mm in diameter were obtained by punching out compressed aerogels or films to be used as binder-free working electrodes. They were directly assembled into the coin cell using neither metallic support nor conductive additives. Lithium metal foil was used as the counter/reference, and 1.2 M LiPF$_6$ in ethylene carbonate and dimethyl carbonate 1/1 (v/v) was used as the electrolyte.

Cyclic voltammetry (CV) curves were registered in a multichannel potentiostat-galvanostat (Biologic VMP3) at a scan rate of 0.1 mV s^{-1}. Electrochemical impedance spectroscopy (EIS) measurements were also carried out in a Biologic VMP3 station within the 100 kHz to 10 mHz frequency range.

Galvanostatic charge and discharge were run in a MACCOR battery tester at different current rates, and the specific capacities were calculated per mass of electrode. It should be pointed out that, in all cases, the specific capacities and current rates are given per mass of the whole electrode and not per mass of silicon as the main active material.

Scheme 1. Schematic Representation of the Synthetic Routes Followed for the Preparation of the A-Si-rGO and F-Si-rGO Samples
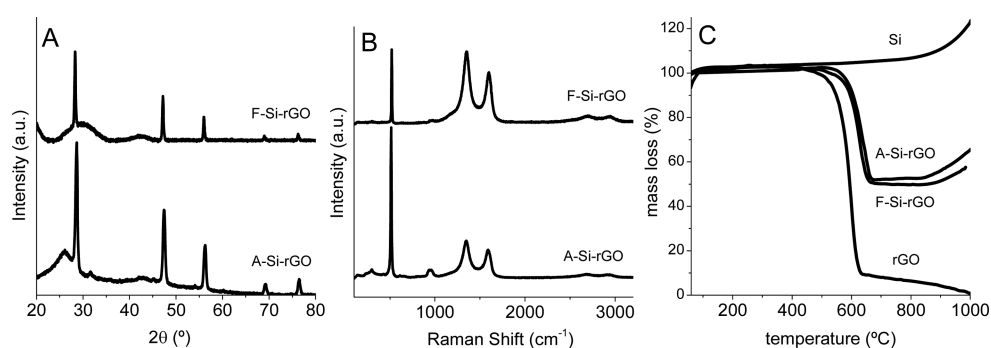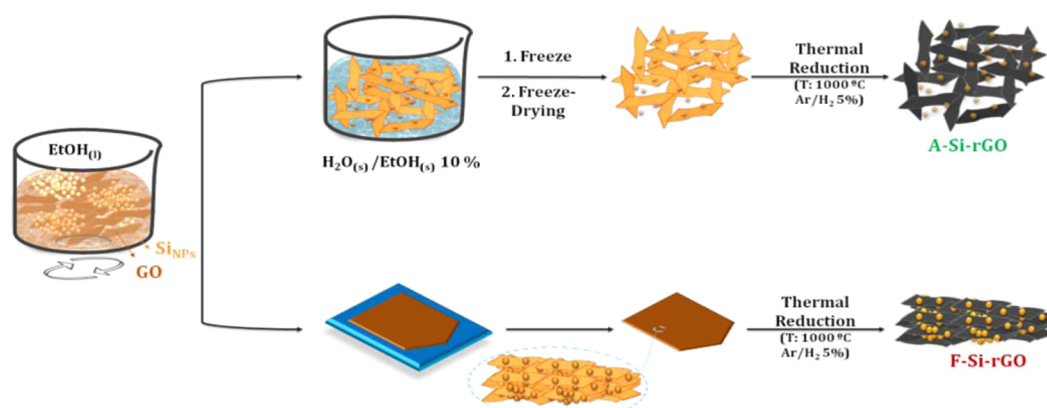

Figure 1. XRD patterns (A), Raman spectra (B), and thermogravimetric curves (C) recorded for labeled samples.

RESULTS AND DISCUSSION

The two different routes followed to process silicon-reduced graphene oxide (Si-rGO) composites in the form of self-standing aerogels (A-Si-rGO) and films (F-Si-rGO) are represented in Scheme 1.

In both cases, a suspension of GO in ethanol was chosen as the media for the mixture to improve the dispersibility of the silicon nanoparticles. As pointed out in the introduction section, previous studies have reported that, to improve the affinity of the silicon nanoparticles with the aqueous graphene oxide suspension, silicon and graphene oxide were sonicated or silicon nanoparticles were exposed to air to be partially oxidized.[27,39]

Use of ethanol as the solvent allows us to obtain a highly homogeneous dispersion of silicon nanoparticles. Digital photographs of silicon nanoparticle-GO suspensions in both water and ethanol after being stirred for 1 day and then left without stirring for 5 days more are shown in Figure S1. It is interesting to note that in the case of the water suspension most of the silicon nanoparticles are deposited at the bottom of the vial, while the suspension in ethanol shows a highly homogeneous brownish dispersion without any evidence of solid precipitates along this period of time.

Free-standing Si-GO aerogels were obtained by suddenly freezing a Si-GO suspension (EtOH/H_2O, 10/90) in liquid nitrogen and then freeze-drying. In the case of the films, a certain amount of suspension was simply casted into a silicon rubber mold and allowed to dry. The reduced samples were obtained by thermal reduction of the samples under an Ar/H_2 (95/5) atmosphere at 1000 °C. Figure 1A shows the XRD

patterns registered for the A-Si-rGO and F-Si-rGO composites. Both patterns show sharp peaks centered at ca. 28.7, 47.5, 56.2, 69.3, and 76.5° that correspond to the (111), (220), (311), (400), and (331) diffraction planes of crystalline silicon in a cubic diamond phase (27−1402 JCPDS card number), respectively. In the case of the A-Si-rGO sample, a quite broad peak centered at ca. 25.5° assigned to the (002) basal diffraction lines in rGO is also observed.[43] The absence of this diffraction peak in the pattern registered for the F-Si-rGO sample could be explained by the small amount and low thickness of the sample used for this particular measurement that enhanced the noise from the sample holder in the form of a broad band between 23 and 34°. The absence of any other diffraction peak apart of those already mentioned was observed, discarding the presence of other crystalline species such as silicon oxide within these samples.

Raman spectra of A-Si-rGO and F-Si-rGO samples depicted in Figure 1B clearly show the D and G bands recorded at 1347 and 1599 cm^{-1} which are ascribed to the existence of defects or edges on disordered carbon and to ordered sp^2 bonded carbon, respectively. Additional peaks centered at ca. 519 cm^{-1} that correspond to silicon are also observed in both samples.[44] No peaks associated with the existence of silicon oxide can be distinguished, suggesting that all of the silicon present in both samples was not oxidized or that it was fully reduced during the thermal treatment. Thermogravimetric analyses performed under an air atmosphere of A-Si-rGO and F-Si-rGO samples are plotted in Figure 1C together with those curves registered for pure silicon nanoparticles and rGO samples. Silicon contents in both aerogel and film composites were calculated from the mass percentage values obtained from their

thermogravimetric curves at 700 °C.[45] At this temperature, most of the carbon from rGO is burnt, and slight increase in the silicon nanoparticles' weight is a consequence of their partial oxidation into SiO_x (4%). Therefore, according to the calculation, the silicon content corresponda to approximately a 40% wt of the composite (41 and 39% wt in the A-Si-rGO and F-Si-rGO samples, respectively). These values match with the starting amount of precursors used for the synthesis.

The microstructure of the samples was evaluated through scanning electron microscopy (SEM) (Figure 2). SEM images
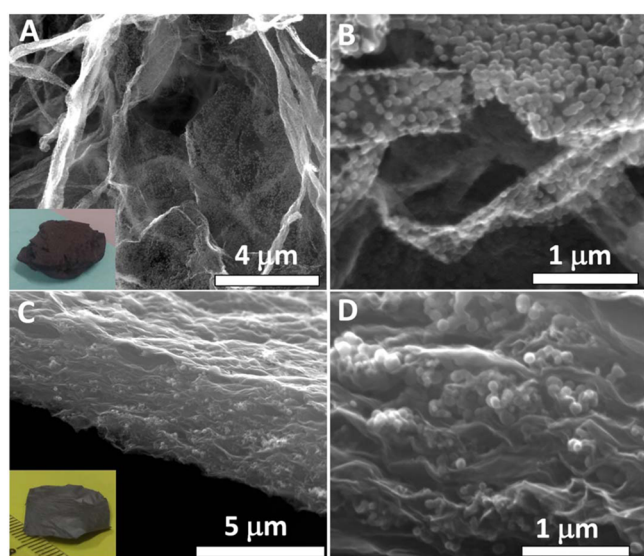

Figure 2. SEM images of A-Si-rGO (A and B) and F-Si-rGO (C and D) at two different magnifications. Insets show digital photograph showing the real aspect of these two samples.

of A-Si-rGO show a highly opened macroporous structure formed by graphene walls homogeneously decorated with small silicon nanoparticles around 50 nm in diameter. This macroporous microstructure is characteristic of ice-templated materials[46,47] in which the macropores are formed from the sublimation of ice. In the case of the A-Si-rGO sample, this porosity appears randomly distributed because the suspension was suddenly frozen and did not allow the preferential growth of the ice crystals. SEM images of the sample processed as film (F-Si-rGO) show a highly packed film obtained by the graphene layer stacking and silicon nanoparticles sandwiched in between them. Figure 2 shows that the level of packing is higher in the case of the film than that in the aerogel, which is evidenced by the larger density measured in the former sample. Taking into account the masses and thicknesses of both aerogels and films, density values of 0.2 and 1.5 g cm^{-3} can be calculated for A-Si-rGO and F-Si-rGO samples, respectively. Although the electrode density is a parameter of paramount importance in the field of energy storage because volumetric energy density is directly related to it, generally, works published on LIBs do not provide this information or discuss it.

Energy dispersive X-ray (EDX) analyses performed in different parts of both samples showed average values of carbon, silicon, and oxygen contents of ca. 58, 39. and 3% in wt, respectively, which are also in agreement with the values of silicon calculated from the thermogravimetric curves.

TEM images registered for the A-Si-rGO and F-Si-rGO confirm the presence of silicon nanoparticles ~50 nm in diameter in the two samples (Figures 3A and C). A closer view of the individual silicon nanoparticles shows the intimate
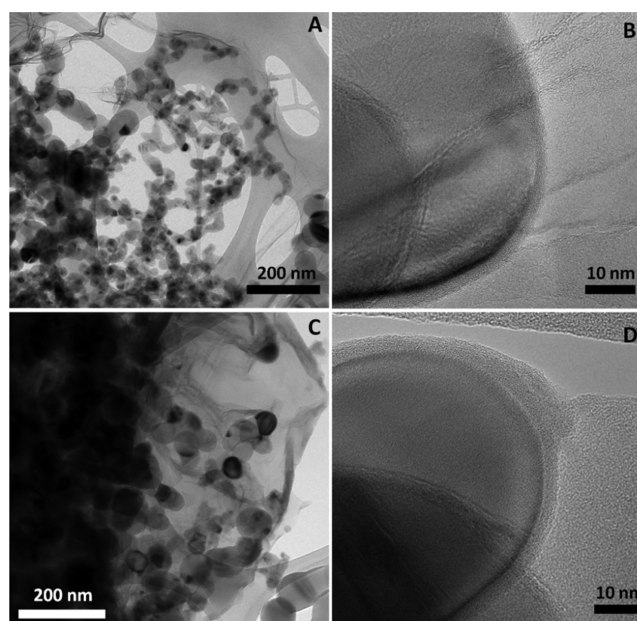

Figure 3. TEM images of A-Si-rGO (A and B) and F-Si-rGO (C and D) at two different magnifications.

contact between the silicon nanoparticles and the reduced graphene oxide sheets in these composites.

Nitrogen adsorption−desorption isotherms were obtained for these two samples (Figure S2). Both of them show a quite similar profile that can be included in the type-II according to the IUPAC classification, which are characteristic of macroporous or nonporous materials. The BET specific surface areas calculated for the F-Si-rGO and A-Si-rGO samples were 26 and 62 m^2 g^{-1}, respectively. The higher specific surface area measured for the sample processed as aerogel should be consequence of the more opened microstructure and to the presence of nanopores with sizes below 6.0 nm, as it was determined from their pore size distributions (Figure S3).

The electrochemical properties of these composites were first evaluated by cyclic voltammetry and impedance spectroscopy. Figures 4A and B show the first four CV cycles registered for A-Si-rGO and F-Si-rGO samples in the range between 0.05 and 2.0 V. Cathodic sweep corresponding to the first cycle of A-Si-rGO (Figure 4A) shows an intense peak centered at ca. 0.65 V that is related to the reaction with the electrolyte and the formation of the SEI. The first cathodic sweep of F-Si-rGO (Figure 4B) also shows a broad shoulder centered at ca. 0.4 V and a shoulder at ca. 0.1 V. The former peak is much less intense compared with the peak observed for A-Si-rGO, suggesting that the SEI is formed in a greater extent in the sample processed as aerogel, and the latter one, which appears as a shoulder, corresponds to the alloying reaction between crystalline silicon and lithium. This low intensity peak was not clearly observed for the A-Si-rGO sample probably because it was shifted toward lower voltages approaching 0.05 V. First anodic sweeps show in both of the samples two peaks centered at ca. 0.25 and 0.48 V, which are ascribed to the lithium dealloying. Second, third, and fourth cycles almost overlap in both cases, showing one major peak centered at ca. 0.19 V in the cathodic sweeps, which correspond to the alloying reaction
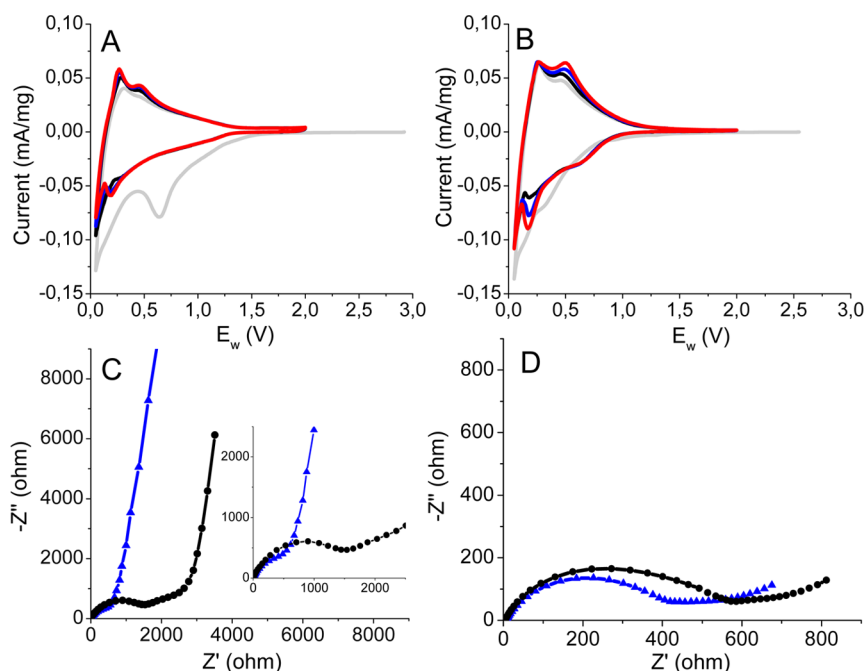
Figure 4. Cyclic voltammetry curves of the samples A-Si-rGO (A) and F-Si-rGO (B) registered for the first four cycles (first, gray; second, black; third, blue; and fourth, red) and the Nyquist plots obtained before cycling (C) and after five cycles (D) of A-Si-rGO (black lines) and F-Si-rGO (blue lines).
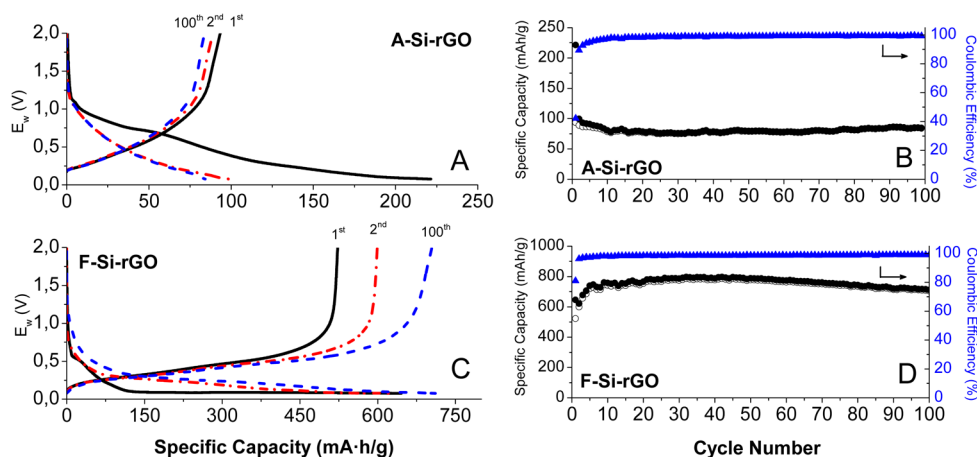

Figure 5. Galvanostatic charge−discharge curves registered for the labeled cycles (A and C) and specific capacities and Coulombic efficiencies (B and D) registered for indicated samples at 50 mA g^{-1} within the 2.0−0.075 V voltage window.

between lithium and amorphous silicon, and two peaks at ca. 0.25 and 0.48 V in the anodic sweeps, which correspond to the delithiation from Li$_x$Si. These profiles are in agreement with the CV reported for similar silicon-based electrodes.[33]

The EIS curves registered for both A-Si-rGO and F-Si-rGO samples before cycling are shown in Figure 4C. Both curves clearly show a depressed semicircle at high frequencies associated with the charge-transfer process, which is associated with the resistance of the SEI.[48] It is worth noting that this semicircle is significantly larger in the spectrum recorded for A-Si-rGO than that for F-Si-rGO, pointing out that the resistance is higher in the former sample as consequence of the formation of the SEI layer in a larger amount within the macroporous electrode. The impedance curve registered for the A-Si-rGO sample also shows a line with a slope of almost 45° at intermediate frequencies related to diffusion processes. EIS curves registered after the fifth cycles (Figure 4D) show many

less differences between both samples, and a decrease in the resistance upon cycling is observed in both cases, indicating that upon the first cycling, the lithium insertion-extraction kinetics was improved.

Galvanostatic charge−discharge curves for the A-Si-rGO and F-Si-rGO samples were registered for the first 100 cycles within the 2.0−0.075 V voltage window (Figure 5). This quite high cutoff voltage was selected because it has been previously reported[49] that increasing the bottom cutoff could help to improve the stability and cyclability of the silicon-based electrodes. The galvanostatic charge−discharge curves revealed that the A-Si-rGO sample was not activated under these specific cycling conditions. The first charge curve of A-Si-rGO shows a plateau around 1.0 V, which is related to the formation of the SEI between the electrolyte and the surface of the electrode. The first charge of A-Si-rGO reached specific capacity of ca. 220 mAh g^{-1}, and the subsequent charge−discharge cycles
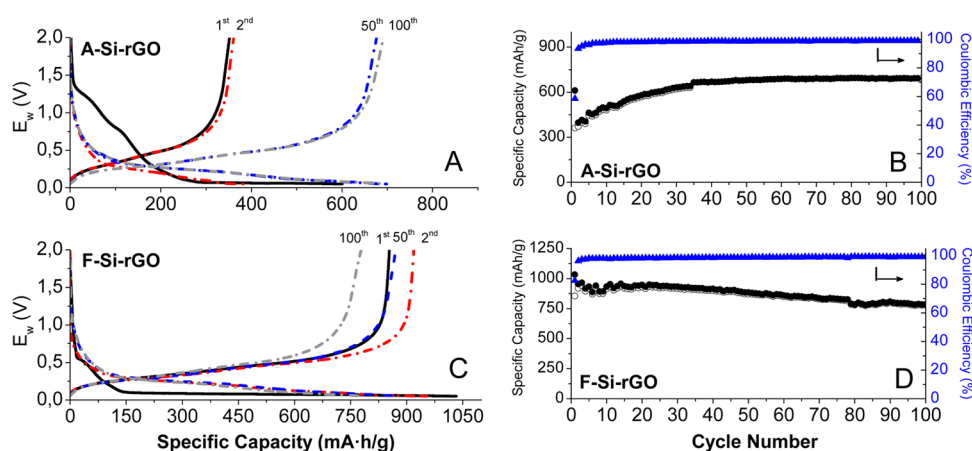
Figure 6. Galvanostatic charge−discharge curves registered for the labeled cycles (A and C) and specific capacities and Coulombic efficiencies (B and D) registered for indicated samples at 50 mA g^{-1} within the 2.0−0.05 V voltage window.

maintained reversible capacities of approximately 85 mAh g^{-1}, which are associated with the reaction between lithium and reduced graphene oxide.

According to the results obtained from SEM, CV, and EIS, we tentatively ascribed the nonactivation of the silicon within the A-Si-rGO composite to its highly open porous microstructure that enhances its reactivity with the electrolyte and favors the formation of the SEI, as observed in the cyclic voltammetry curves. This formation of the SEI may increase the resistance of the electrode and could hinder or avoid the lithium alloying with the silicon nanoparticles at this particular cutoff voltage.

In contrast, the charge−discharge curves of F-Si-rGO under these specific cycling conditions clearly show that the activation of silicon particles took place within this sample (Figures 5C and D). The charge curve corresponding to the first cycle in the F-Si-rGO sample exhibits a profile different than the subsequent ones. The first charge curve shows a plateau at ca. 0.6, much less pronounced than the one observed for the A-Si-rGO sample. This plateau can be ascribed to the SEI formation and the irreversible reaction between the lithium and the functional groups still present within the graphene sheets. A long plateau at ca. 0.08 V, characteristic of the alloying of crystalline silicon with lithium, is also observed during the first charge of the F-Si-rGO sample. The specific capacity calculated from the first charge of the F-Si-rGO sample is ca. 645, and the capacity calculated from the first discharge is ca. 522 mAh g^{-1}, which corresponds to ca. 81% of Coulombic efficiency. Subsequent charge curves show quite similar profiles and a plateau at ca. 0.25 V, characteristic of the lithiation of amorphous silicon. After 20 cycles, reversible stable capacities of around 750 mAh/g$_{electrode}$ were obtained with associated Coulombic efficiencies over 98.5% that were retained or even improved for 100 cycles.

To check the influence that the lower cutoff voltage could have in the stability and capacities of these samples and in an attempt to activate silicon particles within the A-Si-rGO sample, new fresh samples were prepared and tested within the 2.0−0.05 V window. The results are shown in Figure 6. In this particular case, the A-Si-rGO also exhibits a profile characteristic of silicon-based anodes. The first charge curve of the first cycle shows a plateau starting from 1.3 V that is extended to 0.1 V, related to a combination of both the SEI formation and irreversible reaction of lithium with the functional groups of

graphene sheets at higher voltages and reversible lithium reaction with graphene layers. Within this voltage window, the specific capacity per mass of electrode measured for the first charge and discharge reached ca. 600 and 360 mAh g^{-1}, respectively. It is worth highlighting that the subsequent cycles show a progressive increase in the specific capacity values upon cycling, which is stabilized around cycle 35, in which the specific discharge capacity reached a value of ca. 670 mAh g^{-1}. This behavior could be ascribed to the impeded accessibility of lithium to some silicon particles due to the large amount of SEI formed on the surface. After cycle 35, very stable reversible capacities were obtained for more than 60 cycles, and capacities of 692 and 685 mAh g^{-1} with associated Coulombic efficiency of 99% were measured from the charge and discharge curves, respectively.

Galvanostatic charge−discharge curves of the 1st, 2nd, 50th, and 100th cycles recorded for the F-Si-rGO sample in the range between 2.0 and 0.05 V are plotted in Figure 6. They are quite similar to the curves registered for this sample cycled at the upper cutoff voltage. The first charge shows the characteristic profile of the lithiation of crystalline silicon particles. During the first charge, a plateau that starts from 0.6 V and it is extended to 0.1 V is observed. This plateau is related, as in the case of the A-Si-rGO sample, first to the SEI formation and to the reaction between lithium and graphene sheets. Together with it, a long plateau at ca. 0.08 V associated with the alloying of crystalline silicon particles is also observed in this first charge. In this first cycle, charge and discharge specific capacities of 1040 and 865 mAh/g$_{electrode}$ were measured, respectively. These high specific capacitance values calculated per mass of the whole electrodes together with their high first cycle Coulombic efficiencies are among the best values recently reported for graphene-silicon composites as anodes for LIBs (Table S1). Subsequent cycles show similar charge−discharge profiles with a plateau at ca. 0.25 V, which are characteristic of the lithiation of amorphous silicon particles. Specific capacities of 784 and 778 mAh g^{-1} were calculated after 100 cycles from the charge and discharge curves, respectively, with an associated Coulombic efficiency of 99.3%. It is worth mentioning that, within this particular voltage window, the capacity fading observed for the F-Si-rGO sample is larger compared with that of the sample cycled until only 0.075 V, which is in agreement with the existing literature.[50]

For the sake of comparison, another sample denoted as P-Si-rGO was prepared by mixing the Si-rGO composite (80% in
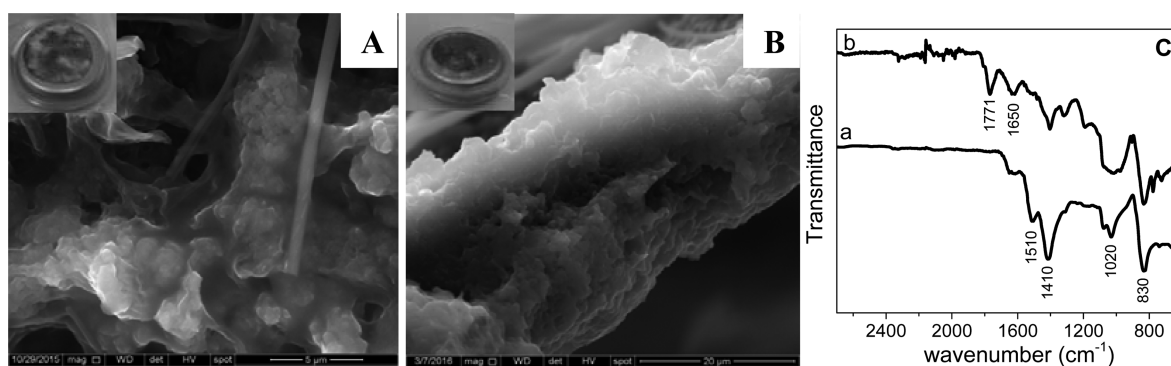
Figure 7. SEM images of A-Si-rGO (A) and F-Si-rGO (B) electrodes cycled 100 times with a bottom cutoff voltage of 50 mV. (C) FT-IR spectra registered for A-Si-rGO (a) and F-Si-rGO (b) samples after 100 cycles. Insets in A and B show the aspect of both electrodes just after the coin cell was disassembled.
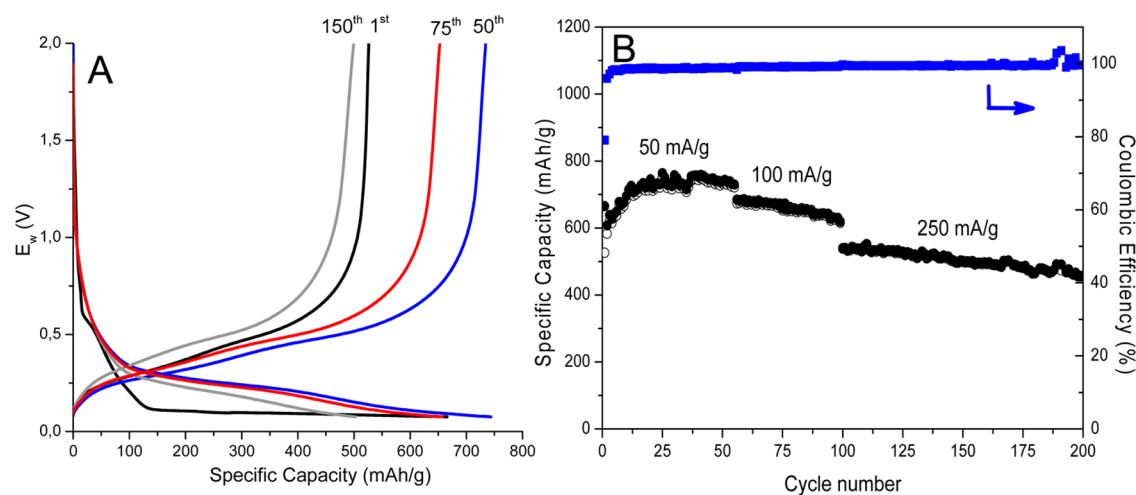

Figure 8. Galvanostatic charge–discharge curves registered in the 1st, 50th, 75th, and 150th cycles. Evolution of the specific capacity of F-Si-rGO cycled for 200 cycles between 2.0 and 0.075 V vs Li at the labeled rates.

wt), carboxymethyl cellulose (CMC) (10% in wt) as a binder, and carbon black (10% in wt) as a conductive additive. This sample was tested under similar conditions, and the results are included in Figure S4. In this case, a specific capacity of 815 mAh g^{-1} with an associated Coulombic efficiency of 76% was measured in the first cycle, and reversible capacities of approximately 600 mAh g^{-1} were obtained in the subsequent 35 cycles. It is worth noticing that longer cycling of P-Si-rGO produces fast capacity fading and the loss of its activity before reaching the 100th cycle. The worse cycling life observed for this sample compared with that measured for the F-Si-rGO and A-Si-rGO self-standing samples is surely associated with the detachment of the silicon particle from the electrodes (Figure S5).

Coin cells of an aerogel and film samples cycled at 50 mA g^{-1} for 100 cycles were disassembled, and the electrodes were characterized by SEM and FT-IR to evaluate the electrode reaction with the electrolyte in each case. Digital images of the electrodes just after opening the cells show that the integrity of these electrodes is maintained after being cycled 100 times. It was also observed that the electrodes were also strongly adhered to the current collector (stainless steel casing), showing a severe electrode/electrolyte reaction during the cycling process. SEM images show that the initial microstructure is maintained in both cases (Figures 7A and B); a more opened structure is still observed in the case of the

aerogel samples, while F-Si-rGO shows a highly packed film. In both cases, the surfaces of the materials appear fully coated by a kind of polymeric layer, and rounded silicon particles can be distinguished through it. In the particular case of the F-Si-rGO, a slight increase in the thickness of the film was observed after being cycled 100 times. It should also be highlighted that, even after 100 cycles at low current rates which enhance the reactivity between electrode surface and the electrolyte, the integrity of the electrodes is preserved, and silicon nanoparticles are not detached from the electrodes. FT-IR spectra show peaks at 830, 1020, 1410, and 1650 cm^{-1} that can be ascribed to lithium ethyl dicarbonate (LiEDC), confirming the presence of species produced by the decomposition of the electrolyte. The infrared spectrum of the F-Si-rGO film also exhibits an intense peak at 1771 cm^{-1}, attributed to the carbonyl stretching bands of some ethylene carbonate, and DMC still presents on this sample. An additional band centered at 1510 cm^{-1} is also observed in the spectrum recorded on the A-Si-rGO sample, which can be related to the presence of Li$_2$CO$_3$, probably formed by the exposure of the sample to air before spectrum acquisition.[51]

To complete the study and evaluate the rate capability of the composite processed as a film, a fresh self-standing F-Si-rGO sample was prepared and cycled at three different current rates (50, 100, and 250 mA/g) within the 2.0−0.075 voltage window. Figure 8 shows the galvanostatic charge−discharge curves

registered in the 1st, 50th, 75th, and 150th cycles and the specific capacity evolution for 200 cycles at the indicated rates. It is worth noticing that the charge−discharge profiles are maintained after the second cycle, and the increasing rate produces a slight decrease in the capacity, which changes from 750, 670, and 500 mAh g^{-1} at 50, 100, and 250 mA g^{-1}, respectively. Increasing the current rate from 50 to 250 mA g^{-1} slightly increases the polarization, as seen in Figure 8B. An increase in the Coulombic efficiency it is also observed as the rate is increased, and values that reach 98.8, 99.0, and 99.5% at 50, 100, and 250 mA g^{-1}, respectively, were measured.

CONCLUSIONS

Here, we presented a very simplistic approach for the fabrication of highly homogeneous silicon-rGO composites processed in the form of both self-standing macroporous aerogels and highly packed films. Use of a GO ethanolic suspension as the media for the preparation of Si-GO composites allowed highly homogeneous materials to be obtained and avoided the oxidation of silicon. These self-standing composites could be directly assembled into the coin cell without adding any binder or using any metallic support to be tested as an anode for LIBs. In this way, we found that the samples processed as aerogels favored the formation of the SEI. This dielectric layer prevented the activation of silicon under certain cycling conditions.

Samples processed as films exhibited quite high densities of ca. 1.5 g cm^{-3} and showed high reversible capacities of 750 mAh/g of the whole electrode (1875 mAh/g of Si) and an areal capacity of ca. 0.7 mAh cm^{-2}. The low irreversible capacity and good stability measured in some of these samples for more than 100 cycles encourage us to perform new experiments to check their potential in a high energy density full cell.

ASSOCIATED CONTENT

ⓢ Supporting Information

The Supporting Information is available free of charge on the ACS Publications website at DOI: 10.1021/acsami.6b07910.

> Digital photographs of suspensions, adsorption−desorption isotherms, pore size distribution, galvanostatic charge−discharge curves, SEM images, and summary of parameters (PDF)

AUTHOR INFORMATION

Corresponding Author

*E-mail: dcarriazo@cicenergigune.com.

Notes

The authors declare no competing financial interest.

ACKNOWLEDGMENTS

REFERENCES

(1) Armand, M.; Tarascon, J.-M. Building Better Batteries. *Nature* **2008**, *451*, 652−657.

(2) Arico, A. S.; Bruce, P.; Scrosati, B.; Tarascon, J. M.; Van Schalkwijk, W. Nanostructured Materials for Advanced Energy Conversion and Storage Devices. *Nat. Mater.* **2005**, *4*, 366−377.

(3) Nitta, N.; Wu, F.; Lee, J. T.; Yushin, G. Li-Ion Battery Materials: Present and Future. *Mater. Today* **2015**, *18*, 252−264.

(4) Dahn, J. R.; Zheng, T.; Liu, Y.; Xue, J. S. Mechanisms for Lithium Insertion in Carbonaceous Materials. *Science* **1995**, *270*, 590−593.

(5) Park, C.-M.; Kim, J.-H.; Kim, H.; Sohn, H.-J. Li-Alloy Based Anode Materials for Li Secondary Batteries. *Chem. Soc. Rev.* **2010**, *39*, 3115−3141.

(6) Goriparti, S.; Miele, E.; De Angelis, F.; Di Fabrizio, E.; Proietti Zaccaria, R.; Capiglia, C. Review on Recent Progress of Nanostructured Anode Materials for Li-Ion Batteries. *J. Power Sources* **2014**, *257*, 421−443.

(7) Obrovac, M. N.; Krause, L. J. Reversible Cycling of Crystalline Silicon Powder. *J. Electrochem. Soc.* **2007**, *154*, A103−A108.

(8) Li, W.; Tang, Y.; Kang, W.; Zhang, Z.; Yang, X.; Zhu, Y.; Zhang, W.; Lee, C.-S. Core−Shell Si/C Nanospheres Embedded in Bubble Sheet-like Carbon Film with Enhanced Performance as Lithium Ion Battery Anodes. *Small* **2015**, *11*, 1345−1351.

(9) Luo, L.; Wu, J.; Luo, J.; Huang, J.; Dravid, V. P. Dynamics of Electrochemical Lithiation/Delithiation of Graphene-Encapsulated Silicon Nanoparticles Studied by In-situ TEM. *Sci. Rep.* **2014**, *4*, 3863.

(10) Obrovac, M. N.; Chevrier, V. L. Alloy Negative Electrodes for Li-Ion Batteries. *Chem. Rev.* **2014**, *114*, 11444−11502.

(11) Liu, G.; Xun, S.; Vukmirovic, N.; Song, X.; Olalde-Velasco, P.; Zheng, H.; Battaglia, V. S.; Wang, L.; Yang, W. Polymers with Tailored Electronic Structure for High Capacity Lithium Battery Electrodes. *Adv. Mater.* **2011**, *23*, 4679−4683.

(12) Koo, B.; Kim, H.; Cho, Y.; Lee, K. T.; Choi, N. S.; Cho, J. A Highly Cross-Linked Polymeric Binder for High-Performance Silicon Negative Electrodes in Lithium Ion Batteries. *Angew. Chem., Int. Ed.* **2012**, *51*, 8762−8767.

(13) Chan, C. K.; Peng, H.; Liu, G.; McIlwrath, K.; Zhang, X. F.; Huggins, R. A.; Cui, Y. High-Performance Lithium Battery Anodes Using Silicon Nanowires. *Nat. Nanotechnol.* **2008**, *3*, 31−35.

(14) Liu, N.; Hu, L.; McDowell, M. T.; Jackson, A.; Cui, Y. Prelithiated Silicon Nanowires as an Anode for Lithium Ion Batteries. *ACS Nano* **2011**, *5*, 6487−6493.

(15) Hu, Y.-S.; Cakan, R.-D.; Titirici, M.-M.; Müller, J.-O.; Schlögl, R.; Antonietti, M.; Maier, J. Superior Storage Performance of a Si@SiOx/C Nanocomposite as Anode Material for Lithium-Ion Batteries. *Angew. Chem., Int. Ed.* **2008**, *47*, 1645−1649.

(16) Liu, N.; Wu, H.; McDowell, M. T.; Yao, Y.; Wang, C.; Cui, Y. A Yolk-Shell Design for Stabilized and Scalable Li-Ion Battery Alloy Anodes. *Nano Lett.* **2012**, *12*, 3315−3321.

(17) Son, I.-H.; Park, J. H.; Kwon, S.; Park, S.; Rümmeli, M. H.; Bachmatiuk, A.; Song, H. J.; Ku, J.; Choi, J. W.; Choi, J.-M.; Doo, S.-G.; Chang, H. Silicon Carbide-Free Graphene Growth on Silicon For Lithium-Ion Battery with High Volumetric Energy Density. *Nat. Commun.* **2015**, *6*, 7393−7401.

(18) Magasinski, A.; Dixon, P.; Hertzberg, B.; Kvit, A.; Ayala, J.; Yushin, G. High-Performance Lithium-Ion Anodes Using a Hierarchical Bottom-up Approach. *Nat. Mater.* **2010**, *9*, 353−358.

(19) Ru, Y.; Evans, D. G.; Zhu, H.; Yang, W. Facile Fabrication of Yolk−Shell Structured Porous Si−C Microspheres as Effective Anode Materials For Li-Ion Batteries. *RSC Adv.* **2014**, *4*, 71−75.

(20) Zhang, J.; Zhang, L.; Xue, P.; Zhang, L.; Zhang, X.; Hao, W.; Tian, J.; Shen, M.; Zheng, H. Silicon-Nanoparticles Isolated by In Situ Grown Polycrystalline Graphene Hollow Spheres for Enhanced Lithium-Ion Storage. *J. Mater. Chem. A* **2015**, *3*, 7810−7821.

(21) Novoselov, K. S.; Geim, A. K.; Morozov, S. V.; Jiang, D.; Zhang, Y.; Dubonos, S. V.; Grigorieva, I. V.; Firsov, A. A. Electric Field Effect in Atomically Thin Carbon Films. *Science* **2004**, *306*, 666−669.

(22) Zhou, X.; Yin, Y.-X.; Wan, L.-J.; Guo, Y.-G. Self-Assembled Nanocomposite of Silicon Nanoparticles Encapsulated in Graphene through Electrostatic Attraction for Lithium-Ion Batteries. *Adv. Energy Mater.* **2012**, *2*, 1086−1090.

(23) Li, Y.; Yan, K.; Lee, H.-W.; Lu, Z.; Liu, N.; Cui, Y. Growth of Conformal Graphene Cages on Micrometre-Sized Silicon Particles as Stable Battery Anodes. *Nature Energy* **2016**, *1*, 15029−15037.

(24) Yu, G.; Xie, X.; Pan, L. J.; Bao, Z.; Cui, Y. Hybrid Nanostructured Materials for High-Performance Electrochemical Capacitors. *Nano Energy* **2013**, *2*, 213−234.

(25) Vargas, O.; Caballero, A.; Morales, J.; Rodríguez-Castellón, E. Contribution to the Understanding of Capacity Fading in Graphene Nanosheets Acting as an Anode in Full Li-Ion Batteries. *ACS Appl. Mater. Interfaces* **2014**, *6*, 3290–3298.

(26) Chou, S.-L.; Wang, J.-Z.; Choucair, M.; Liu, H.-K.; Stride, J. A.; Dou, S.-X. Enhanced Reversible Lithium Storage in a Nanosize Silicon/Graphene Composite. *Electrochem. Commun.* **2010**, *12*, 303–306.

(27) Lee, J. K.; Smith, K. B.; Hayner, C. M.; Kung, H. H. Silicon Nanoparticles–Graphene Paper Composites for Li Ion Battery Anodes. *Chem. Commun.* **2010**, *46*, 2025–2027.

(28) Wang, J.; Zhong, C.; Chou, S.; Liu, H. K. Flexible Free-Standing Graphene-Silicon Composite Film for Lithium-Ion Batteries. *Electrochem. Commun.* **2010**, *12*, 1467–1470.

(29) Chen, D.; Yi, R.; Chen, S.; Xu, T.; Gordin, M. L.; Wang, D. Facile Synthesis of Graphene–Silicon Nanocomposites with an Advanced Binder for High-Performance Lithium-Ion Battery Anodes. *Solid State Ionics* **2014**, *254*, 65–71.

(30) Liu, B.; Wang; Chen, X.; Wang, H.; Chen, Z.; Cheng, Y.-B.; Zhou, C.; Shen, G. Hierarchical Silicon Nanowires-Carbon Textiles Matrix as a Binder-Free Anode for High-Performance Advanced Lithium-Ion Batteries. *Sci. Rep.* **2013**, *3*, 1622.

(31) Wang, B.; Li, X.; Zhang, X.; Luo, B.; Jin, M.; Liang, M.; Dayeh, S. A.; Picraux, S. T.; Zhi, L. Adaptable Silicon–Carbon Nanocables Sandwiched between Reduced Graphene Oxide Sheets as Lithium Ion Battery Anodes. *ACS Nano* **2013**, *7*, 1437–1445.

(32) Li, F.; Yue, H.; Yang, Z.; Li, X.; Qin, Y.; He, D. Flexible Free-Standing Graphene Foam Supported Silicon Films as High Capacity Anodes for Lithium Ion Batteries. *Mater. Lett.* **2014**, *128*, 132–135.

(33) Tang, H.; Zhang, Y. J.; Xiong, Q. Q.; Cheng, J. D.; Zhang, Q.; Wang, X. L.; Gu, C. D.; Tu, J. P. Self-Assembly Silicon/Porous Reduced Graphene Oxide Composite Film as a Binder-Free and Flexible Anode for Lithium-Ion Batteries. *Electrochim. Acta* **2015**, *156*, 86–93.

(34) Son, I. H.; Park, J. H.; Kwon, S.; Choi, J. W.; Rümmeli, M. H. Graphene Coating of Silicon Nanoparticles with CO_2-Enhanced Chemical Vapor Deposition. *Small* **2016**, *12*, 658–667.

(35) Evanoff, K.; Magasinski, A.; Yang, J.; Yushin, G. Nanosilicon-Coated Graphene Granules as Anodes for Li-Ion Batteries. *Adv. Energy Mater.* **2011**, *1*, 495–498.

(36) Kannan, A. G.; Kim, S. H.; Yang, H. S.; Kim, D.-W. Silicon Nanoparticles Grown on a Reduced Graphene Oxide Surface as High-Performance Anode Materials for Lithium-Ion Batteries. *RSC Adv.* **2016**, *6*, 25159–25166.

(37) Lee, W. J.; Hwang, T. H.; Hwang, J. O.; Kim, H. W.; Lim, J.; Jeong, H. Y.; Shim, J.; Han, T. H.; Kim, J. Y.; Choi, J. W.; Kim, S. O. N-Doped Graphitic Self-Encapsulation for High Performance Silicon Anodes in Lithium-Ion Batteries. *Energy Environ. Sci.* **2014**, *7*, 621–626.

(38) Zhang, F.; Yang, X.; Xie, Y.; Yi, N.; Huang, Y.; Chen, Y. Pyrolytic Carbon-Coated Si Nanoparticles on Elastic Graphene Framework as Anode Materials for High-Performance Lithium-Ion Batteries. *Carbon* **2015**, *82*, 161–167.

(39) Zhou, X.; Yin, Y.-X.; Wan, L.-J.; Guo, Y.-G. Facile Synthesis of Silicon Nanoparticles Inserted into Graphene Sheets as Improved Anode Materials for Lithium-Ion Batteries. *Chem. Commun.* **2012**, *48*, 2198–2200.

(40) Ji, J.; Ji, H.; Zhang, L. L.; Zhao, X.; Bai, X.; Fan, X.; Zhang, F.; Ruoff, R. S. Graphene-Encapsulated Si on Ultrathin-Graphite Foam as Anode for High Capacity Lithium-Ion Batteries. *Adv. Mater.* **2013**, *25*, 4673–4677.

(41) Botas, C.; Álvarez, P.; Blanco, C.; Santamaría, R.; Granda, M.; Ares, P.; Rodríguez-Reinoso, F.; Menéndez, R. The Effect of the Parent Graphite on the Structure of Graphene Oxide. *Carbon* **2012**, *50*, 275–282.

(42) Botas, C.; Carriazo, D.; Singh, G.; Rojo, T. Sn– and SnO_2–Graphene Flexible Foams Suitable as Binder-Free Anodes for Lithium Ion Batteries. *J. Mater. Chem. A* **2015**, *3*, 13402–13410.

(43) Cui, P.; Lee, J.; Hwang, E.; Lee, H. One-Pot Reduction of Graphene Oxide at Subzero Temperatures. *Chem. Commun.* **2011**, *47*, 12370.

(44) Chen, Y.; Du, N.; Zhang, H.; Yang, D. Firmly Bonded Graphene–Silicon Nanocomposites as High-Performance Anode Materials for Lithium-Ion Batteries. *RSC Adv.* **2015**, *5*, 46173–46180.

(45) Luo, J.; Zhao, X.; Wu, J.; Jang, H. D.; Kung, H. H.; Huang, J. Crumpled Graphene-Encapsulated Si Nanoparticles for Lithium Ion Battery Anodes. *J. Phys. Chem. Lett.* **2012**, *3*, 1824–1829.

(46) Gutiérrez, M. C.; Ferrer, M. L.; del Monte, F. Ice-Templated Materials: Sophisticated Structures Exhibiting Enhanced Functionalities Obtained after Unidirectional Freezing and Ice-Segregation-Induced Self-Assembly. *Chem. Mater.* **2008**, *20*, 634–648.

(47) Nardecchia, S.; Carriazo, D.; Ferrer, M. L.; Gutiérrez, M. C.; del Monte, F. Three Dimensional Macroporous Architectures and Aerogels Built of Carbon Nanotubes and/or Graphene: Synthesis and Applications. *Chem. Soc. Rev.* **2013**, *42*, 794–830.

(48) Wang, C.; Appleby, A. J.; Little, F. E. Electrochemical Impedance Study of Initial Lithium Ion Intercalation Into Graphite Powders. *Electrochim. Acta* **2001**, *46*, 1793–1813.

(49) Obrovac, M. N.; Christensen, L. Structural Changes in Silicon Anodes during Lithium Insertion/Extraction. *Electrochem. Solid-State Lett.* **2004**, *7*, A93–A96.

(50) Cui, L. F.; Ruffo, R.; Chan, C. K.; Peng, H.; Cui, Y. Crystalline-Amorphous Core–Shell Silicon Nanowires for High Capacity and High Current Battery Electrodes. *Nano Lett.* **2009**, *9*, 491–495.

(51) Pérez-Villar, S.; Lanz, P.; Schneider, H.; Novák, P. Characterization of a Model Solid Electrolyte Interphase/Carbon Interface by Combined in Situ Raman/Fourier Transform Infrared Microscopy. *Electrochim. Acta* **2013**, *106*, 506–515.